

Geologic characteristics of the Chang'E-3 exploration region[†]

ZHAO JianNan, HUANG Jun^{*}, QIAO Le, XIAO ZhiYong, HUANG Qian, WANG Jiang,
HE Qi & XIAO Long^{*}

Planetary Science Institute, China University of Geosciences, Wuhan 430074, China

Received January 17, 2014; accepted January 18, 2014; published online January 22, 2014

We present topographic, geomorphologic and compositional characteristics of a $1^{\circ} \times 1^{\circ}$ ($\sim 660 \text{ km}^2$) region centered near the landing site of Chang'E-3 using the highest spatial resolution data available. We analyze the topography and slope using Digital Terrain Model (DTM) generated from Terrain Camera (TC) images. The exploration region is overall relatively flat and the elevation difference is less than 300 m, and the slopes of 80% area are less than 5° . Impact craters in the exploration region are classified into four types based on their degradation states. We investigate the wrinkle ridges visible in the exploration region in detail using TC and Lunar Reconnaissance Orbiter (LRO) Narrow Angle Camera (NAC) images. We calculate FeO and TiO_2 abundances using Multispectral Imager (MI) data, and confirm two basaltic units: the northern part belongs to Imbrian low-Ti/very-low-Ti mare basalts, and the southern part is Eratosthenian low-Ti/high-Ti mare basalts. Finally, we produce a geological map and propose the geologic evolution of the exploration region. We also suggest several rover traverses to explore interesting targets and maximize the potential scientific output.

Chang'E-3, Yutu rover, traverse planning, geological map, Mare Imbrium, the Moon

PACS number(s): 96.20.Br, 96.20.Dt, 96.20.Ka, 96.30.Bc, 95.55.Pe

Citation: Zhao J N, Huang J, Qiao L, et al. Geologic characteristics of the Chang'E-3 exploration region. *Sci China-Phys Mech Astron*, 2014, 57: 569–576, doi: 10.1007/s11433-014-5399-z

1 Introduction

Nearly 40 years after the completion of the Apollo and Luna missions, the third Chinese lunar mission, Chang'E-3 (CE-3), was launched on December 2, 2013 and safely landed on the surface of the Moon on December 14, 2013. The rover “Yutu” separated from the lander successfully about 8 h later. The landing site of CE-3 is 340.49°E , 44.12°N , which is located in the northern part of Mare Imbrium (Figure 1). As the first Chinese lunar soft-lander and rover, the landing site is selected primarily considering engineering constraints including topography, communication and solar illumination. In addition, local geologic diversity

is also taken into consideration, including impact craters, wrinkle ridges, and basaltic materials that have different ages. The CE-3 landing site and its nearby terrains have never been visited by any other missions. Therefore, the exploration will shed light on the geologic characteristics, geochemical diversity and evolution of Mare Imbrium.

Geological maps in Apollo era [1] and recent studies [2–4] reveal regional geologic information for Sinus Iridum and the adjacent terrains. However, the spatial resolution of previous maps is not sufficient for detailed geologic study or for the rover traverse planning considering both scientific and engineering requirements. Luckily, as unprecedented high spatial resolution remote sensing data being acquired by recent lunar missions (e.g., Chang'E 1 & 2, SELENE-1, Chandrayaan-1 and Lunar Reconnaissance Orbiter: LRO), large scale geological mapping and detailed study are possible for CE-3 landing site and its exploration region. In this

^{*}Corresponding author (HUANG Jun, email: junhuang@cug.edu.cn; XIAO Long, email: longxiao@cug.edu.cn)

[†]Contributed by XIAO Long (Associate Editor)

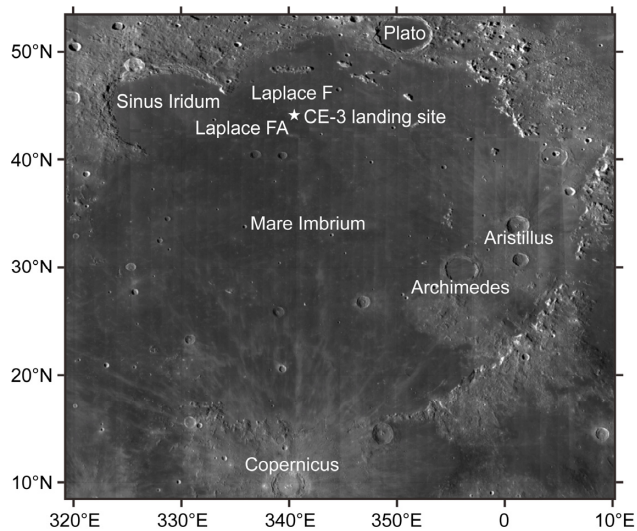


Figure 1 Location of CE-3 landing site (labeled by the star) within the Mare Imbrium. Background is LRO Wide Angle Camera image mosaic in a simple cylindrical projection.

study, we mapped an area of $1^\circ \times 1^\circ$ ($\sim 660 \text{ km}^2$) centered near CE-3 landing site (Figure 2). We also presented topographic, geomorphologic, and elemental results of the exploration region. The results will support the traverse planning and assist Yutu rover to select interesting detecting targets.

2 Geologic backgrounds

The study area is located in the northern Mare Imbrium, about 140 km east to Sinus Iridum (Figure 1). Two named impact craters are in the adjacent regions: Laplace F, with a diameter of 5.7 km, is 26 km away; and Laplace FA with diameter of 2.5 km and 1 km away from the landing site respectively. There are two main stratigraphic units in the study area according to the geological map of the Sinus Iridum quadrangle compiled by Schaber [1], the unit in the north of the area is assigned as Im1 (Imbrian mare materials 1) while the other unit in the middle and south is EIm (Eratosthenian-Imbrian mare materials). However, subsequent age dating carried out by Hiesinger et al. [5], Bugiolacchi and Guest [6], and Qiao et al. [4] all confirmed that the unit Im1 is older than 3.2 Ga and the unit EIm is younger than 3.0 Ga. Therefore we renamed F unit Im1 as Im (Imbrian mare materials) and EIm as Em (Eratosthenian mare materials).

Previous studies have made detailed analyses of geologic features in Mare Imbrium such as lava flows and wrinkle ridges. Schaber [7] studied the characteristics of lava flows in Mare Imbrium and proposed the thickness of Eratosthenian phase-III lava flow is 10–65 m with an average of 30–35 m. The eruptive source region was interpreted as in

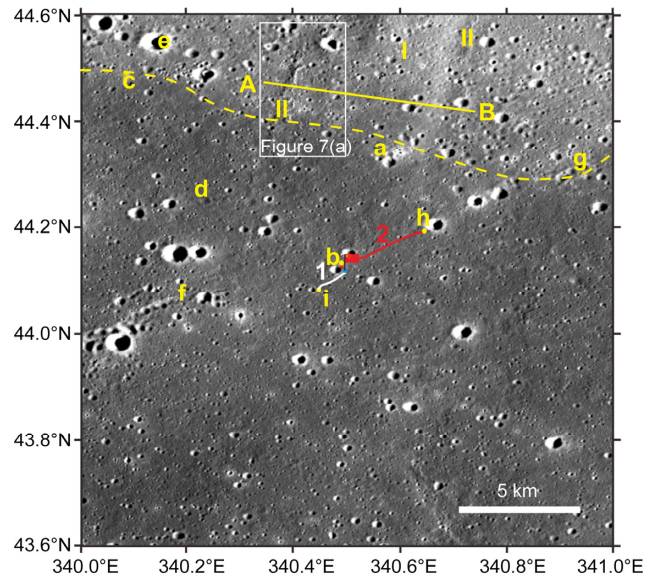


Figure 2 (Color online) TC Morning Map of the study area in a simple cylindrical projection (TCO_MAPm04_N45E339N42E342SC). The flag denotes the landing site of CE-3. “a–d” are craters of different degradation states. “e” is the largest crater in this area. “f & g” are chain craters. “h” is a crater that may have excavated materials of unit Im. “i” is the nearest rayed crater from CE-3 landing site. “I” represents the broad gentle ridge while “II” represents the narrow sharp ridges. Line “AB” is the profile line across the ridges. Dashed line is the boundary of unit Im and Em. “1 & 2” are suggested traverse plans for the Yutu rover.

the south-southwest corner of Imbrium Basin. Hiesinger [8] also calculated the thickness of Eratosthenian lava flow ranging from 32 m to 50 m. Moore and Schaber [9] estimated the yield strength of lava flows in Mare Imbrium to be 100–200 Pa, the maximum average flow rate to be 5–14 km/h and the density to be 3.0 g/cm^3 . Lucchitta [10] studied the morphology of wrinkle ridges in Mare Imbrium and suggested that the origin of the ridges maybe associate with volcanic activity and faults. Xu et al. [11] proposed that the concentric ridges in Mare Imbrium are controlled by the structure of the Imbrium basin and the north-south trending ridges may result from the combination of basin structure and regional stress field.

3 Data & methods

3.1 Topography

High spatial resolution topographic information is critical to the rover traverse planning. The vertical measurement accuracy of foot print of Lunar Orbiter Laser Altimeter (LOLA) onboard LRO can reach 0.1 m and the interval is 25 m. Gridded data derived from LOLA has a spatial resolution of 20 m along track and $\sim 0.07^\circ$ cross track [12]. Haruyama et al. [13] produced global Digital Terrain Model (DTM) using stereo pair images of Terrain Camera (TC)

onboard SELENE-1, and its spatial resolution is ~ 10 m/pixel. The TC topographic model has been compared to the laser altimeter data of SELENE-1 and the 1σ difference is 3.2 m. In this study, we analyzed the topography of the CE-3 exploration region using TC DTM due to its better spatial resolution than LOLA gridded data at $\sim 44^\circ\text{N}$. We also calculated the surface slope in a 3×3 analysis windows using difference computation with TC DTM.

3.2 Geomorphology analysis

We use images obtained from the Wide Angle Camera (WAC) and Narrow Angle Camera (NAC) of LRO and TC of SELENE-1 to study the geomorphology. The spatial resolution of WAC images is 100 m/pixel [14]. The mosaic of WAC images shows albedo differences and serves as background. NAC images have a spatial resolution of 0.5 m/pixel, and we use them to study the small scale geologic features in detail. TC images have different illumination conditions, and moderate spatial resolution (10 m/pixel) [15]. They are used to study moderate geomorphologic features and provide a local context for NAC images.

3.3 Rock types

Mare Imbrium is mostly covered by basalts. FeO and TiO_2 abundances are significant in geological unit classification, rock type identification and lunar resource estimation. Lucey et al. [16] presented an algorithm to calculate FeO and TiO_2 abundances using Clementine Ultraviolet/Visible (UVVIS) data. However, the Clementine UVVIS data do not cover a large portion of the study area and the average spatial resolution is only 115 m/pixel. Multispectral Imager (MI) onboard SELENE-1 acquires multispectral data at higher spatial resolution (~ 20 m/pixel). Otake et al. [17] developed an algorithm to derive FeO and TiO_2 abundances using five bands (415 nm, 750 nm, 900 nm, 950 nm, 1000 nm) of MI data:

$$\theta_{\text{Ti}} = \arctan\{[(R_{415}/R_{750}) - 0.208]/[R_{750} - (-0.108)]\}, \quad (1)$$

$$\text{wt}\%\text{TiO}_2 = 0.72 \times \theta_{\text{Ti}}^{14.964}, \quad (2)$$

$$\theta_{\text{Fe}} = -\arctan\{[(R_{950}/R_{750}) - 1.250]/(R_{750} - 0.037)\}, \quad (3)$$

$$\text{wt}\%\text{FeO} = 20.527 \times \theta_{\text{Fe}} - 12.266, \quad (4)$$

where R_{415} , R_{950} and R_{750} are reflectance of MI data at 415 nm, 950 nm and 750 nm. θ_{Fe} and θ_{Ti} are angle parameters related to FeO and TiO_2 abundances. The standard deviations of FeO and TiO_2 abundances derived from the algorithm are 0.81wt% and 0.43wt% respectively. We derived FeO and TiO_2 abundances for the study region using MI data, because the results have a higher spatial resolution and a better coverage.

4 Results

4.1 Topography

Surface topographic difference is less than 300 m for the whole study area (Figure 3). The middle and southern parts are higher in elevation, while the northwest and northeast are lower. The lowest point in the study area is -2850 m, located within an impact crater of northwest, and the highest point is located in the south (-2560 m). The lander is located on the continuous impact ejecta deposits of a small crater, and the local elevation is about -2610 m.

According to the slope map derived from the TC DTM (Figure 4), 80% of the study area is relatively flat (less than 5°). The terrain slopes near impact craters are larger, and the steepest part is inner walls of impact craters (more than 20°). The landing site of CE-3 is about 5° , which is suitable for

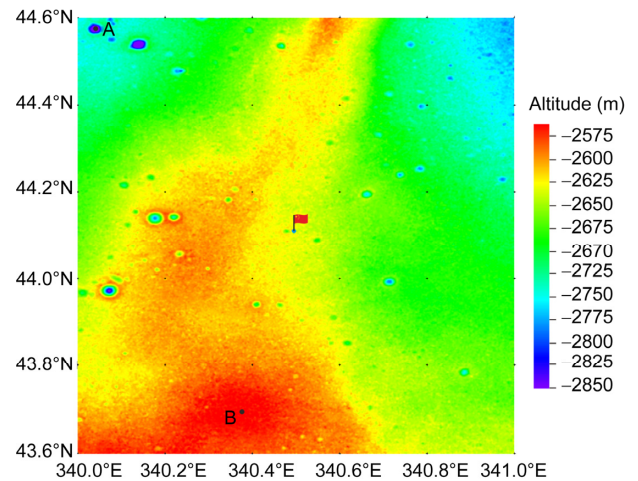


Figure 3 Topographic map of the study area (DTM_MAP_02_N45E339-N42E342SC). The flag denotes the landing site of CE-3. “A” and “B” are the lowest and highest points in the area.

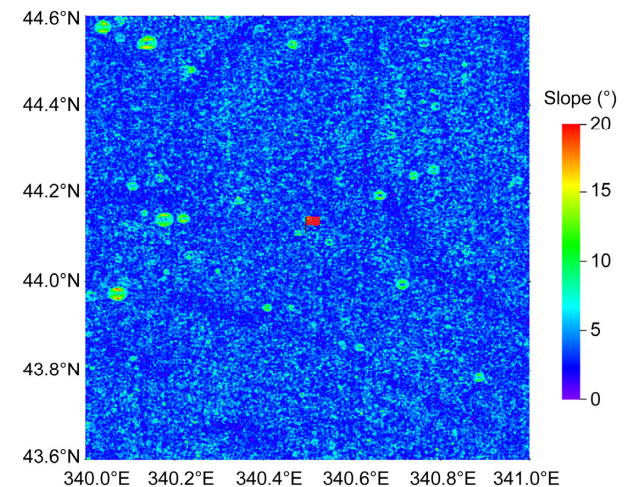


Figure 4 Slope map of the study area. The flag denotes the landing site of CE-3.

the exploration of the rover.

4.2 Geomorphology

4.2.1 Impact crater

Impact craters in the study area are simple bowl-shape craters with diameters less than 2 km. The biggest impact crater (“e” in Figure 2) of the study area is located in the northwest, with a diameter of ~ 1.1 km and a depth of ~ 170 m.

Based on the degradation states, we divided the impact craters within the study area into four types. The first type craters have radial bright rays and are very fresh. They are thought to be formed in Copernican [18]. These craters usually have sharp and raised rims, and a large amount of

boulders can be observed near the rims and on the slopes of the crater walls. The crater shown in Figure 5(a) is an example of the Type 1 craters in this region. It locates at 340.60°E , 44.34°N , with a diameter of ~ 200 m and a depth of 35 m. The depth/diameter (d-D) ratio is ~ 0.18 and the slope of the inner wall is $\sim 27^\circ$. We observed over 10 rays and the longest one extends over 400 m. On the other hand, numerous boulders are found within and near the crater. We can barely identify a cone-shape structure in the center with a basal diameter of ~ 30 m and a height of ~ 5 m. This structure may differ from the ordinary central peaks of impact craters, because central peak craters on the Moon usually occur at 10–150 km in diameter [19].

The second type craters are relatively fresh, with large slope of the inner wall and high d-D ratios, but they don't

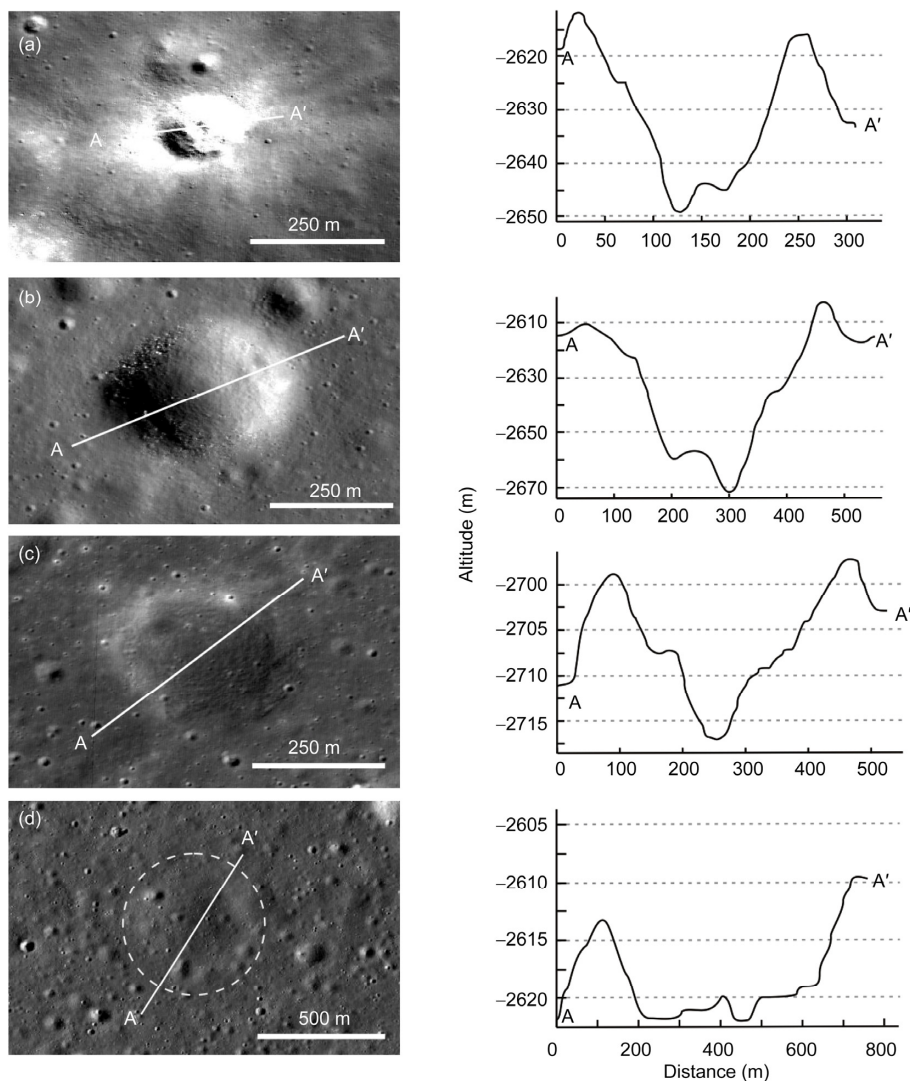


Figure 5 Four types of craters of different degradation states and their elevation profiles measured from TC DTM. (a) A fresh rayed crater (Type 1, centered at 340.60°E , 44.34°N , NAC: M183661683RE). (b) A slightly degraded crater (Type 2, centered at 340.48°E , 44.12°N , NAC: M181302794LE). (c) A largely degraded crater (Type 3, centered at 340.09°E , 44.46°N , NAC: M190738378LE). (d) A ghost crater (Type 4, centered at 340.23°E , 44.25°N , NAC: M17757954LE). White solid lines “AA'” in (a)–(d) are profile lines. White dashed line in (d) is the possible outline of the ghost crater. Locations of these craters are labeled in Figure 2.

have bright rays. They have circular shapes and raised rims, but the rims are less sharp than those of the Type 1 craters. Type 2 craters might be formed in Copernican or Eratosthenian. The impact crater to the west of CE-3 landing site (Figure 5(b)) is an example of Type 2. It is centered at 340.48°E, 44.12°N with a diameter of ~420 m and a depth of 68 m (d-D ratio: ~0.16). The rim is ~20 m higher than the adjacent terrains. Boulders in the crater may also suggest a relatively young impact age.

The third type craters have modified appearances and usually do not have boulders in the wall and near the rim. They are older than craters of Type 1 and Type 2. Type 3 craters are not always circular in shape, but modified to irregular shapes by mass wasting, later impact cratering and lava infilling. The crater in Figure 5(c) is an example of Type 3 craters. It locates at 340.09°E, 44.46°N, with a diameter of 400 m and depth of 20 m, with a d-D ratio of ~0.05.

The fourth type craters are severely modified by subsequent degradation events and they are usually called “ghost” craters. It is very difficult to identify them from the images, since they don't have obviously-identified elevated or completed rims. Figure 5(d) (centered at 340.23°E, 44.25°N) is an example of Type 4 craters. Its diameter is 450 m and the depth is 10 m (d-D ratio: ~0.02). Type 4 craters are thought to be formed earliest in the study area.

We also identified many impact crater chains (e.g., “f & g” in Figure 2). The length of the chains can reach 10 km. The elongated shapes of these craters indicate they are second craters generated by ejecta of larger craters. We suspect the ejecta were from big Copernican craters such as Aristillus, Aristarchus and Copernicus based on the general direction of the elongation of the clusters.

4.2.2 Wrinkle ridges

More than five wrinkle ridges can be recognized in the study area. The biggest one (“I” in Figure 2) lies in the north and extends along N-S direction. In general, a typical wrinkle ridge is composed of two parts: a broad gentle arch in the base and an overlying sharper and more contorted ridge [20,21]. However, we did not observe sharp ridges on Ridge I. The width of Ridge I varies along its strike. The northern part is the widest that has a basal width of ~8 km and a top width of ~3.5 km. The elevation differences between the top of the ridge and the mare surface decrease from ~80 m to ~40 m from the north to the south of the ridge. We plotted the profile of Ridge I with LOLA data (Figure 6), and it has a convex shape. The slope of the western flank is ~1.1° and that of the eastern flank is ~2.8°. The flank slope of the southern part gradually decreases to the south while the regional altitude increases. The wrinkle ridge disappears in the center of the region, and only a small part can be observed in the southernmost part of the study area (Figure 2).

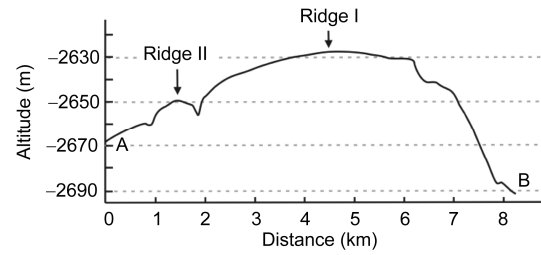


Figure 6 Elevation profile of Ridge I and II from LOLA data. The profile line is “AB” shown in Figure 2.

We also recognized several narrow and sharp ridges (“II” in Figure 2) on the flanks of Ridge I with TC and LRO NAC images. These small ridges extend in N-S direction. They rose ~10–15 m over the surrounding terrains and the flank slopes can be greater than 15°.

We have estimated the formation and activity sequence of Ridges I and II based on the crosscutting and superposition relationship between craters and ridges. Both Ridge II and Ridge I occur on unit Im and Em, it implies that they formed after the emplacement of Eratosthenian mare basalt. As Ridge II lies on the flanks of Ridge I, Ridge I is probably older than Ridge II. We observed some relatively young craters were destroyed by Ridge II (Figure 7), while many highly degraded craters were on the top of Ridge I. It indicates that the activity of Ridge II postdates that of Ridge I.

4.3 Element abundances and rock types

There are two rock types and further divided into two basaltic units (Figure 8). Unit Em (middle and southern part) has

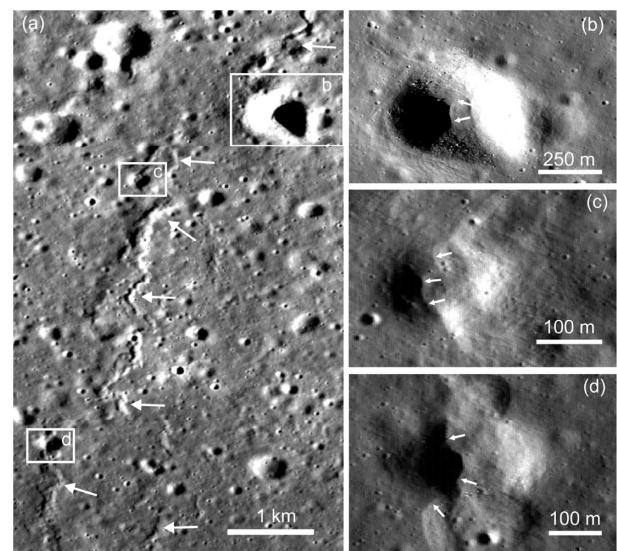


Figure 7 Destruction of craters due to the activity of Ridge II. (a) Aerial view of a part of Ridge II (indicated by white arrows, the range has been shown in Figure 2, TC: TCO_MAPm04_N45E339N42E342SC). (b)–(d) Craters that were partly destroyed by Ridge II and white arrows indicate the edge of the ridges (NAC: M181302794LE).

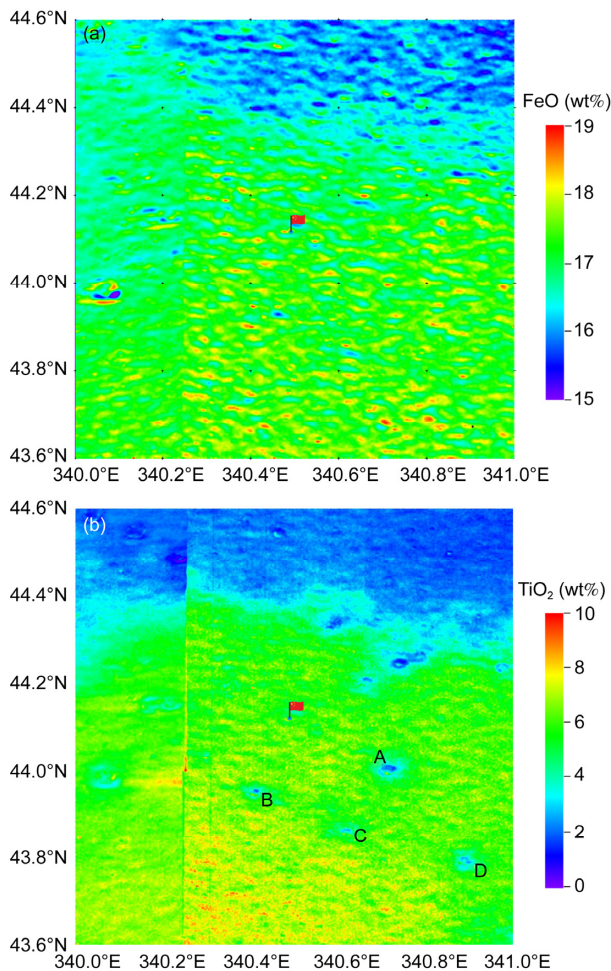


Figure 8 FeO (a) and TiO₂ (b) abundances in the study area (MI_MAP_02_N45E340N44E341SC and MI_MAP_02_N44E340N43E341SC: artifacts can be seen in the left portion of the original data). The flag denotes the landing site of CE-3. “A–D” in (b) are craters that have obviously lower TiO₂ abundance.

both elevated FeO (~18%) and TiO₂ (5%–10%) abundances. Unit Im (northern part) has lower abundances (FeO: ~16%, TiO₂: <4%). Based on the classification of mare basalt [22]: high-Ti (>6wt% TiO₂), low-Ti (1–6wt% TiO₂), very-low-Ti (VLT, <1wt% TiO₂), the materials in unit Im are low-Ti/VLT basalt and that in unit Em are low-Ti/high-Ti basalt. From the TiO₂ abundance map, we can identify some large and relatively fresh impact craters (Crater A–D in Figure 8(b)) have lower TiO₂ values than their surrounding terrains in unit Em, which indicates that they have penetrated into unit Em and exposed/excavated underlying materials of unit Im. Therefore, the thickness of basalt of unit Em can be roughly estimated by measuring the depths of the craters mentioned above. The depths of these four craters (measured from TC DTM) are all larger than 70 m, then the thickness of unit Em is probably less than 70 m in the southern and central area of the region. This result is generally consistent with previous studies (Schaber [7]: 10–63 m;

Hiesinger [8]: 32–50 m). We hope the penetrating radar on Yutu rover can verify the thickness of unit Em.

4.4 Geological map and possible evolution of the CE-3 exploration region

We produced a geological map of the exploration region based on the results presented above (Figure 9). There are two units of basaltic materials: Em and Im. Qiao et al. [4] reported absolute model ages (AMAs) derived from crater size-frequency distribution on top of these two units: the unit Em is 2.5 Ga and the unit Im is 3.32 Ga. The AMAs are largely consistent with previous studies (Hiesinger et al. [5]: Em 2.96 Ga and Im 3.52 Ga; Bugiolacchi and Guest [6]: Em 2.22 Ga and Im 3.31 Ga). We adopt the ages of Qiao et al. [4] as the AMAs of unit Em and Im. Four types of impact craters have been identified based on degradation states as mentioned above, and we labeled them as C₁, C₂, C₃ and C₄ with the order of degradation levels (e.g., C₁ represents the freshest Type 1 craters and C₄ denotes the most degraded Type 4 craters). The crater chains/clusters are labeled as Ccsc (clustered satellitic crater materials), which follows the nomenclature tradition of lunar geological maps [1].

We propose a possible evolution of the study area as the following: basaltic lava of unit Im filled the Imbrium impact basin ~3.32 Ga ago forming the oldest unit exposed in this area. In the following 0.8 Gyr, several volcanic event occurred within the Imbrium Basin [5,6], but the study area was not affected by these resurfacing events. At ~2.5 Ga, ~70 m thick basaltic lava filled the middle to southern part of the study area to form the unit Em. Afterwards, Ridge I formed followed by the formation of Ridge II. Ridge II was active till very recently. Finally, ejecta of larger impact craters (e.g., Aristillus) created the crater chains/clusters.

5 Discussion

5.1 Formation mechanism of wrinkle ridges in the study area

The origin of wrinkle ridges on the Moon has been extensively studied. Some researchers supported that wrinkle ridges are volcanic features such as fissure volcanoes as they are identified only in lunar maria region [20,23,24]. Others advocated that ridges result from tectonic activity such as folds and faults. However, different tectonic patterns were also proposed [10,25,26]. The origin of ridges can also be a combination of volcanic and tectonic activity [21,27]. Recent studies support the tectonic origin of the wrinkle ridges, including large-scale folds beneath the surface [28] and an underlying reverse fault with an upper anticline [29].

Wrinkle ridges in the study area belong to the N-S ridge system in Mare Imbrium. Previous studies proposed that the

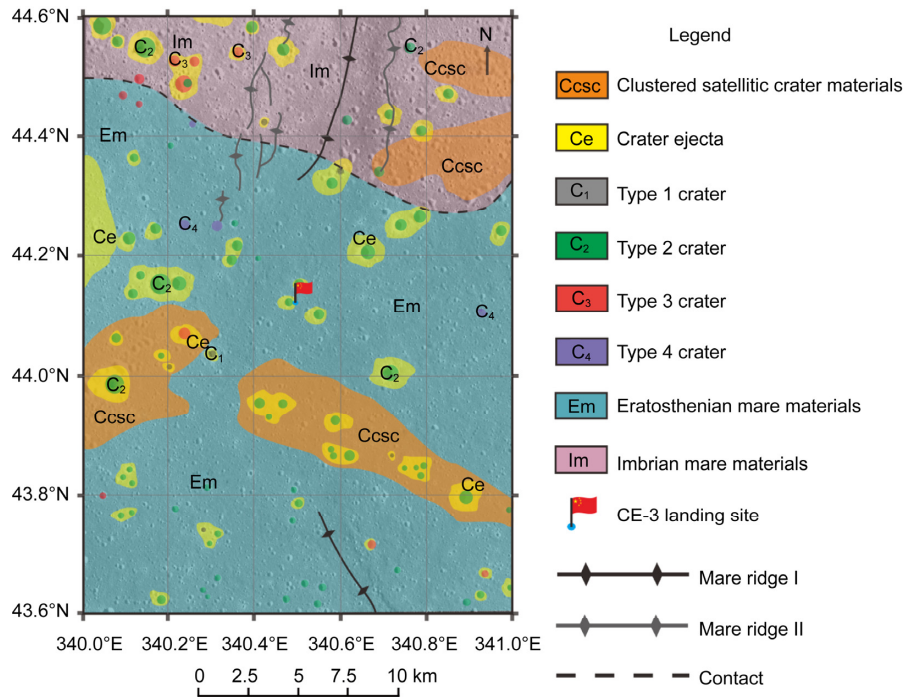


Figure 9 Geological map of the CE-3 exploration region. The background image is a TC Morning Map in Lambert projection (TCO_MAPm04_N45E339N42E342SC).

origin of the N-S ridge system was related to the subsidence of the maria and global contraction [11,30]. Two subclasses of wrinkle ridges (Ridge I and Ridge II) have been identified and they may have different formation and activity times (see sect. 4.2.2). Ridge I formed after the emplacement of Eratosthenian mare basalts and it was inactive for a much longer time than Ridge II. We favor subsidence of maria and global contraction as the formation mechanism of Ridge I, due to the cease of maria subsidence at ~1.2 Ga [31]. Ridge II formed after Ridge I and it has been active till very recently (Figure 8). We favor late-stage contraction of the Moon as the origin of Ridge II due to the similarity of young lobate scarps revealed by recent studies [32,33].

5.2 Rover traverse planning

The Yutu rover is equipped with Panorama Camera, Visible/Near Infrared Imager, Alpha Particle X-Ray Spectrometer and Ground-Penetrating Radar. These scientific instruments can be used to take images and analyze mineralogy and chemistry of the lunar surface, and identify the subsurface structure of the lunar crust. The designed working period for the rover is 3 months, and the working distance is ~3 km around the landing site and could be rove further during the possible extended exploration phase. In order to maximum the potential scientific outputs after numerous engineering constraints, we propose two traverses for the rover.

Path 1 is for the rover to explore the nearest Type 1 im-

compact crater which is ~1.5 km from the landing site (“i” in Figure 2). Type 1 impact craters are the freshest and youngest on the Moon because their bright rays are visible. The reason for the different albedo of the rays from surrounding terrains remains debatable [34]. The instruments onboard the rover may distinguish the unknown reasons from surface roughness, different space weathering and compositional heterogeneity. It will be the first time to provide “ground truth” for the albedo differences.

Path 2 is for the rover to ride to the rim of Crater “h” which is ~3.5 km from the landing site (Figure 2). First we can study the morphology of Crater “b” in Figure 2 and observe the degradation state. Then we are able to study the subsurface structure of the traverse, including regolith thickness, lava flow thickness and faults. Finally, Crater “h” have possibly dug out the materials of Im, and it will be an opportunity to study the lower TiO₂ abundance basaltic materials and provide clues for the magma evolution of Mare Imbrium in both space and time.

6 Summary

We made a comprehensive analysis of the geologic characteristics of the CE-3 exploration region with high-quality remote-sensing data obtained by LRO and SELENE. Surface topography of the area is relatively flat and the slopes are less than 5° in 80% of the area. Crater morphology is studied and four types of impact craters are identified based

on their degradation states. Wrinkle ridges with possibly different formation mechanisms and active periods are observed and classified into two types (Ridges I and II). We propose that the formation mechanism of Ridge I is the subsidence of maria and global contraction while Ridge II is related to the late-stage contraction of the Moon. According to the FeO and TiO₂ abundances, two main rock types are found: low-Ti/ very-low-Ti mare basalts in Unit Im and low-Ti/ high-Ti mare basalts in Unit Em. Thickness of the Em unit is estimated to be less than 70 m. We produced a geological map and reconstructed a possible geological evolutionary history. We also suggested two traverses for the exploration of Yutu rover.

This work was supported by the National Natural Science Foundation of China (Grant No. 41373066), the Key Research Program of the Chinese Academy of Sciences (Grant No. KGZD-EW-603), Specialized Research Fund for the Doctoral Program of Higher Education (SRFDP) (Grant No. 20130145130001) and China Postdoctoral Science Foundation (Grant No. 2013M540614).

- 1 Schaber G G. Geologic Map of the Sinus Iridum Quadrangle of the Moon, I-602. Washington D C: US Geological Survey, 1969
- 2 Chen S, Meng Z, Cui T, et al. Geologic investigation and mapping of the Sinus Iridum quadrangle from Clementine, SELENE, and Chang'e-1 data. *Sci China-Phys Mech Astron*, 2010, 53(12): 2179–2187
- 3 Ding X, Han K, Pang J, et al. Digital geological mapping of Sinus Iridum area of the Moon based on the Chang'E-I data. *Acta Geol Sin-Engl*, 2013, 87(6): 1643–1657
- 4 Qiao L, Xiao L, Zhao J, et al. Geological features and magmatic activities history of sinus Iridum, the moon (in Chinese). *Sci Sin-Phys Mech Astron*, 2013, 43(11): 1370–1386
- 5 Hiesinger H, Jaumann R, Neukum G, et al. Ages of mare basalts on the lunar nearside. *J Geophys Res-Planets*, 2000, 105(E12): 29239–29275
- 6 Bugiolacchi R, Guest J. Compositional and temporal investigation of exposed lunar basalts in the Mare Imbrium region. *Icarus*, 2008, 197(1): 1–18
- 7 Schaber G G. Lava flows in Mare Imbrium: Geologic evaluation from Apollo orbital photography. *Geochim Cosmochim Ac*, 1973, 1(Suppl): 73–92
- 8 Hiesinger H. Lunar mare basalt flow units: Thicknesses determined from crater size-frequency distributions. *Geophys Res Lett*, 2002, 29(8): 89
- 9 Moore H, Schaber G. An estimate of the yield strength of the Imbrium flows. In: *Proceedings of the Sixth Lunar Science Conference*. Houston: Lunar and Planetary Institute, 1975. 101–118
- 10 Lucchitta B K. Topography, structure, and mare ridges in southern Mare Imbrium and northern Oceanus Procellarum. In: *Proceedings of the Eighth Lunar Science Conference*. Houston: Lunar and Planetary Institute, 1977. 2691–2703
- 11 Xu Y, Yan D, Yu T, et al. Distribution characteristics and controlling factors of lunar mare ridges in Mare Imbrium (in Chinese). *Front Earth Sci*, 2012, 19(6): 060–071
- 12 Smith D E, Zuber M T, Neumann G A, et al. Initial observations from the Lunar Orbiter Laser Altimeter (LOLA). *Geophys Res Lett*, 2010, 37(18): L18204
- 13 Haruyama J, Hara S, Hioki K, et al. Lunar global digital terrain model dataset produced from SELENE (Kaguya) terrain camera stereo observations. In: *43rd Lunar and Planetary Science Conference*. Houston: Lunar and Planetary Institute, 2012. 1200
- 14 Robinson M S, Brylow S M, Tschimmel M, et al. Lunar Reconnaissance Orbiter Camera (LROC) instrument overview. *Space Sci Rev*, 2010, 150(1–4): 81–124
- 15 Haruyama J, Matsunaga T, Ohtake M, et al. Global lunar-surface mapping experiment using the Lunar Imager/Spectrometer on SELENE. *Earth Planets Space*, 2008, 60(4): 243–255
- 16 Lucey P G, Blewett D T, Jolliff B L. Lunar iron and titanium abundance algorithms based on final processing of Clementine ultraviolet-visible images. *J Geophys Res-Planets*, 2000, 105(E8): 20297–20305
- 17 Otake H, Ohtake M, Hirata N. Lunar iron and titanium abundance algorithms based on SELENE (Kaguya) Multiband Imager data. In: *43rd Lunar and Planetary Science Conference*. Houston: Lunar and Planetary Institute, 2012. 1905
- 18 McEwen A S, Moore J M, Shoemaker E M. The Phanerozoic impact cratering rate: Evidence from the farside of the Moon. *J Geophys Res-Planets*, 1997, 102(E4): 9231–9242
- 19 Greeley R. *Planetary Landscapes*. 2nd ed. London: Chapman and Hall Ltd, 1994. 44
- 20 Strom R G. Lunar mare ridges, rings and volcanic ring complexes. In: *The Moon, Proceedings from IAU Symposium no. 47*. Dordrecht: International Astronomical Union, 1972. 187–215
- 21 Yue Z, Ouyang Z, Li H, et al. The origin and geological significance of lunar ridges. *Chin J Geochem*, 2007, 26(4): 418–424
- 22 Neal C R, Taylor L A. Petrogenesis of mare basalts: A record of lunar volcanism. *Geochim Cosmochim Ac*, 1992, 56(6): 2177–2211
- 23 Fielder G, Kiang T. The segmental structure of wrinkle ridges and the lunar grid system. *Observatory*, 1962, 82: 8–9
- 24 Hartmann W K, Wood C A. Moon: Origin and evolution of multi-ring basins. *Moon*, 1971, 3(1): 3–78
- 25 Golombek M P, Anderson F S, Zuber M T. Martian wrinkle ridge topography: Evidence for subsurface faults from MOLA. *J Geophys Res-Planets*, 2001, 106(E10): 23811–23821
- 26 Sharpton V, Head J. Lunar mare ridges: Analysis of ridge-crater intersections and implications for the tectonic origin of mare ridges. In: *Proceedings of the 18th Lunar and Planetary Science Conference*. Houston: Lunar and Planetary Institute, 1988. 307–317
- 27 Young R A, Brennan W J, Wolfe R W, et al. Analysis of lunar mare geology from Apollo photography. *Geochim Cosmochim Ac*, 1973, 1(Suppl): 57–71
- 28 Ono T, Kumamoto A, Nakagawa H, et al. Lunar radar sounder observations of subsurface layers under the nearside maria of the Moon. *Science*, 2009, 323(5916): 909–912
- 29 Schultz R, Nahm A, Montési L. Wrinkle ridges on Mars: Absence of décollement tectonics. In: *EGU General Assembly 2010*. Vienna: European Geosciences Union, 2010. 1969
- 30 Solomon S C, Head J W. Lunar mascon basins: Lava filling, tectonics, and evolution of the lithosphere. *Rev Geophys*, 1980, 18(1): 107–141
- 31 Watters T R, Schultz R A. *Planetary Tectonics*. Cambridge: Cambridge University Press, 2010. 121
- 32 Banks M E, Watters T R, Robinson M, et al. Morphometric analysis of small-scale lobate scarps on the Moon using data from the Lunar Reconnaissance Orbiter. *J Geophys Res-Planets*, 2012, 117: E00H11
- 33 Watters T R, Robinson M S, Beyer R A, et al. Evidence of recent thrust faulting on the Moon revealed by the Lunar Reconnaissance Orbiter Camera. *Science*, 2010, 329(5994): 936–940
- 34 Hawke B R, Blewett D T, Lucey P G, et al. The origin of lunar crater rays. *Icarus*, 2004, 170(1): 1–16